PCCP

PAPER

View Article Online
View Journal | View Issue

Cite this: *Phys. Chem. Chem. Phys.*, 2015, **17**, 7857

Atomic-scale origin of piezoelectricity in wurtzite ZnO†

Jung-Hoon Lee,*[a] Woo-Jin Lee,[a] Sung-Hoon Lee,[b] Seong Min Kim,[a] Sungjin Kim[a] and Hyun Myung Jang*[cd]

Received 29th December 2014,
Accepted 11th February 2015

DOI: 10.1039/c4cp06094f

www.rsc.org/pccp

ZnO has been extensively studied by virtue of its remarkably high piezoelectric responses, especially in nanowire forms. Currently, the high piezoelectricity of wurtzite ZnO is understood in terms of the covalent-bonding interaction between Zn 3d and O 2p orbitals. However, the Zn 3d orbitals are not capable of forming hybridized orbitals with the O $2p_z$ orbitals since the Zn ion is characterized by fully filled non-interacting 3d orbitals. To resolve this puzzling problem, we have investigated the atomic-scale origin of piezoelectricity by exploiting density-functional theory calculations. On the basis of the computed orbital-resolved density of states and the band structure over the Γ–M first Brillouin zone, we propose an intriguing bonding mechanism that accounts for the observed high piezoelectricity – intra-atomic $3d_{z^2}$–$4p_z$ orbital self-mixing of Zn, followed by asymmetric hybridization between the Zn $3d_{z^2}$–$4p_z$ self-mixed orbital and the O $2p_z$ orbital along the polar c-axis of the wurtzite ZnO.

1. Introduction

Piezoelectricity is an electromechanical phenomenon in which an electric dipole is generated by an external mechanical stress (and *vice versa*). Owing to this tendency of the electromechanical coupling, piezoelectric materials have received a great deal of attention[1–8] and are crucial in a variety of different applications that include piezoelectric sensors and motors, ultrasonic and medical imaging devices, and microactuators. Renowned examples of piezoelectrics that have been extensively studied are $BaTiO_3$,[9] $PbTiO_3$,[10] $Pb(Zr_{1-x}Ti_x)O_3$,[11] $PbMg_{1/3}Nb_{2/3}O_3$–$PbTiO_3$ (PMN-PT),[12,13] $Pb(Zn_{1/3}Nb_{2/3})O_3$–$PbTiO_3$ (PZN-PT),[13] $BiFeO_3$,[14] III–V wurtzite nitrides,[15] and wurtzite oxides.[16–20]

Among numerous piezoelectrics currently under investigation, III–V wurtzite nitrides and oxides are considered to be two most promising candidates for practical applications of lead-free piezoelectric materials. In particular, wurtzite ZnO has been extensively studied by virtue of its high piezoelectric tensor.[16–20] Moreover, ZnO nanostructures show a variety of different morphological configurations that include nanowires,[21] nanobelts,[22] nanosprings,[23] nanorings,[24] nanobows,[25] and nanohelices.[26] Among these nanostructures, nanowires exhibit remarkably enhanced piezoelectric responses. According to previous experimental results,[27] the piezoelectric coefficient of the ZnO nanowire with a diameter of 230 nm is as high as 1200 pm V^{-1} which is two orders of magnitude larger than that of the bulk ZnO (9.93 pm V^{-1}). Because of this, ZnO nanowires are considered to be the most promising candidate of nanogenerators in the field of energy harvesting. On the basis of first-principles calculations, Agrawal *et al.*[28] recently showed that the observed giant piezoelectric responses of ZnO nanowires mainly stem from the size effects. In spite of extensive experimental[21–29] and theoretical[16,17,20,30–33] studies on its piezoelectric properties and technological applications, however, little progress has been made in our fundamental understanding of the microscopic origin of piezoelectricity in the wurtzite ZnO.

Polar ZnO possesses the hexagonal $P6_3mc$ space-group symmetry. This polar structure is characterized by the absence of mirror planes that are perpendicular to the c-axis. Thus, ferroelectricity might be expected in the wurtzite ZnO with its polarization vector along the unique c-axis of $P6_3mc$.[16] In reality, however, the ferroelectric dipole switching does not occur up to its melting point of ~1975 °C. This unusual observation can be attributed to a very large activation energy needed for the dipole switching across the two degenerate off-centering positions.[18] In the wurtzite structure, each Zn ion is tetrahedrally coordinated with four O atoms, forming a tetrahedral unit [Fig. 1(a)]. The center of the positive charge (Zn ion) is displaced with respect to that of the negative charges along the c-axis.

[a] *Samsung Advanced Institute of Technology (SAIT), Samsung Electronics, Suwon 443-742, Republic of Korea. E-mail: jhlee.david@gmail.com*
[b] *Center for Artificial Low Dimensional Electronic Systems, Institute for Basic Science, Pohang 790-784, Republic of Korea*
[c] *Division of Advanced Materials Science (AMS) and Department of Materials Science and Engineering, Pohang University of Science and Technology (POSTECH), Pohang 790-784, Republic of Korea. E-mail: hmjang@postech.ac.kr; Tel: +82-54-279-2819*
[d] *Department of Physics, Pohang University of Science and Technology (POSTECH), Pohang 790-784, Republic of Korea*

† Electronic supplementary information (ESI) available: Calculated ground-state atomic positions of ZnO and density of states (DOS) and partial density of states (PDOS) obtained using the hybrid functionals. See DOI: 10.1039/c4cp06094f

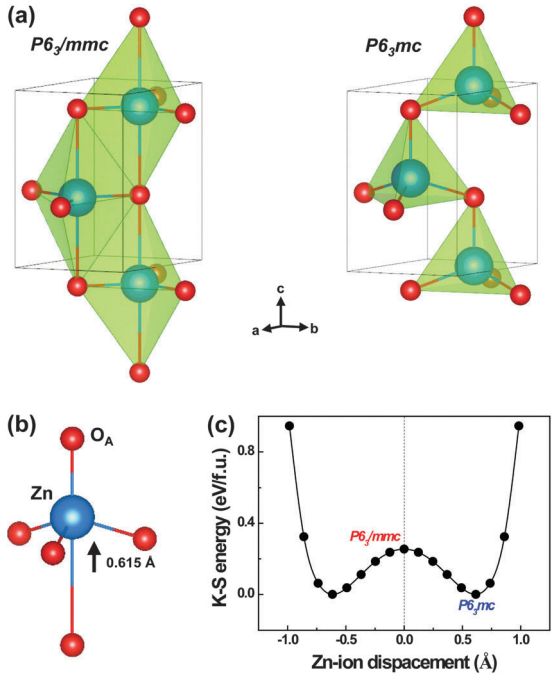

Fig. 1 Crystal and off-centering structures of ZnO. (a) Comparison of the nonpolar $P6_3/mmc$ structure (left) with the polar $P6_3mc$ structure (right). (b) The ZnO_5 unit in the polar $P6_3mc$ structure. The black arrow denotes the direction of the off-centered displacement (OCD) in the ZnO_5 unit. (c) The computed double-well potential plotted as a function of the Zn-ion displacement from the centrosymmetric position.

This creates a *c*-axis-oriented electric dipole moment in each tetrahedral unit [Fig. 1(b)]. When a strain is applied along the *c*-axis, the dipole moment is substantially enhanced by the deformation of the tetrahedral unit. This strong strain–phonon coupling consequently leads to large piezoelectric coefficients.[9] According to the previous first-principles study,[17] the hybridization between Zn 3d and O 2p orbitals is the origin of the observed strain–phonon coupling, thus, of large piezoelectric coefficients in the wurtzite ZnO. In other words, the covalent-bonding interaction between Zn 3d and O 2p orbitals plays a major role in the manifestation of piezoelectricity. However, the Zn 3d orbitals are not capable of forming hybridized orbitals with the axial O (O_A) $2p_z$ orbitals since Zn ions are characterized by fully filled non-interacting 3d orbitals, namely, (Ar core) 3d.[10] The present context is similar to chemically inert noble gas elements (such as Ne or Ar) having fully filled non-interacting s and p orbitals.

Considering the above puzzling problem associated with the Zn 3d–O 2p covalent-bonding interaction, it is of great scientific importance to clearly elucidate the atomic-scale origin of piezoelectricity and associated chemical bonding in the wurtzite ZnO. Accordingly, the main purpose of the present study is to resolve the above-mentioned dilemma by exploiting first-principles density-functional theory (DFT) and density-functional perturbation theory (DFPT) calculations. On the basis of *ab initio* calculations of the orbital-resolved band structure and density of states, we propose a new bonding mechanism directly responsible for triggering piezoelectricity in the wurtzite ZnO. This can be summarized as intra-atomic $3d_{z^2}$–$4p_z$ orbital self-mixing of Zn, followed by asymmetric hybridization between the Zn $3d_{z^2}$–$4p_z$ self-mixed orbital and the O_A $2p_z$ orbital along the *c*-axis of $P6_3mc$.

2. Computational details

To elucidate the piezoelectric origin of ZnO, we performed *ab initio* DFT calculations on the basis of the generalized gradient approximation (GGA) and the GGA + *U* method implemented with the projector augmented wave (PAW)[34,35] pseudopotential using the Vienna *ab initio* Simulation Package (VASP).[36,37] We adopted (i) a 7 × 7 × 5 Monkhorst-Pack *k*-point mesh centered at *Γ*,[38] (ii) a 500 eV plane-wave cutoff energy, and (iii) the tetrahedron method with the Blöchl corrections for the Brillouin zone integrations.[39] The Hubbard U_{eff} of 8 eV on Zn 3d states was chosen on the basis of experimental results. When U_{eff} = 8.0 eV, the position of the Zn 3d level is in good agreement with the experimental range which is between −8 and −7 eV below the valence-band top.[40] This enables us to make an accurate analysis on the bonding nature of ZnO. We explicitly treated 12 valence electrons for Zn ($3d^{10}4s^2$) and 6 for O ($2s^22p^4$). All structural relaxations were performed with a Gaussian broadening of 0.05 eV.[41] The ions were relaxed until the forces on them were less than 0.005 eV $Å^{-1}$. The piezoelectric tensor was calculated using the methods of DFPT.[42–44]

3. Results and discussion

In Fig. 1(a), we compare the computationally optimized structural units of the wurtzite ($P6_3mc$) unit cell with those of the nonpolar $P6_3/mmc$ unit cell (see the ESI†). The experimentally obtained lattice parameters[45] were used in the DFT calculations (*a* = 3.2418 Å and *c* = 5.1877 Å). The wurtzite structure with $P6_3mc$ symmetry is known as the ground-state structure of ZnO, while the nonpolar $P6_3/mmc$ structure is less stable than the polar $P6_3mc$ structure and can be stabilized by an imposed strain. The $P6_3/mmc$ structure is commonly called a 'graphitic-like structure'.[46–48] This nonpolar structure possesses zero piezoelectric coefficients (e_{33} and e_{31}) since both Zn and O atoms are located on the same *a*–*b* plane, and consequently the electric dipole is removed (Table 1). In the present calculations, thus, we adopt the $P6_3/mmc$ structure as a reference structure.

The main difference between the $P6_3/mmc$ and $P6_3mc$ structures is that, in the nonpolar $P6_3/mmc$ phase, all ions are restricted within the planes that are parallel to the *a*–*b* basal plane, whereas the mirror planes perpendicular to the *c*-axis disappear in the polar $P6_3mc$ structure. As shown in the computed structure of the ZnO_5 unit [Fig. 1(b)], the electric

Table 1 Comparison of the calculated e_{33} and e_{31} components of the piezoelectric tensor (in units of C m^{-2}) of the $P6_3/mmc$ and $P6_3mc$ structures with the experimental values

	This work		Experiment[50]	
	e_{33}	e_{31}	e_{33}	e_{31}
$P6_3mc$	1.01	−0.50	0.96	−0.62
$P6_3/mmc$	0	0		

dipole moment originates from the vertical shift of the Zn ion with respect to the centre of the surrounding oxygen cage. Thus, the net dipole moment develops along the *c*-axis of $P6_3mc$. The computed Kohn–Sham (K–S) energy plotted as a function of the Zn-ion off-centering displacement (OCD) demonstrates the stability of the polar $P6_3mc$ phase over the centrosymmetric $P6_3/mmc$ phase [Fig. 1(c)]. According to the computed double-well potential, the difference in the thermodynamic stability between the two phases is 0.255 eV per formula unit, with a remarkably large net OCD of 0.615 Å for the central Zn ion.

We have then accurately determined the piezoelectric tensor by exploiting the *ab initio* DFPT calculations. The computed piezoelectric coefficients (e_{33} and e_{31}) for the $P6_3/mmc$ and $P6_3mc$ structures are listed in Table 1. The spontaneous polarization along the *c*-axis, P_3, can be expressed *via* e_{33} and e_{31} as

$$\delta P_3 = e_{33}\varepsilon_3 + e_{31}(\varepsilon_1 + \varepsilon_2) \quad (1)$$

where ε_1 and ε_3 are the strains along the *a*-axis and the *c*-axis, respectively. In eqn (1) we ignore the nonlinear (second order) terms that are proportional to the product of ε_j and ε_k. This nonlinear effect is known to make a substantial contribution to the piezoelectric polarization of highly strained systems such as quantum wells, wires and dots.[49,50] By restricting our analysis of the piezoelectric origin to bulk piezoelectrics under small strains, we can deliberately remove the nonlinear effect in our subsequent analysis.

The Berry-phase polarization calculations predict that P_3 for the $P6_3mc$ structure is -0.03 C m^{-2}.[51] This value is consistent with previous calculations.[20] The calculated e_{33} (1.01 C m^{-2}) for the $P6_3mc$ phase is also in good agreement with the experimental e_{33} value (0.96 C m^{-2}),[52] as shown in Table 1. The magnitude of the calculated e_{31} (0.50 C m^{-2}) for the $P6_3mc$ phase is somewhat smaller than that of the experimental e_{31} value (0.62 C m^{-2}). In the case of the $P6_3/mmc$ structure, both e_{33} and e_{31} are zero. Thus, there is no dipole moment induced by the external strain along the *c*-axis in the nonpolar $P6_3/mmc$ structure. As mentioned previously, this graphitic-like structure is an ideal reference system.

In Fig. 2, we show a purely electronic contribution to e_{33} plotted as a function of the Zn-ion OCD. On the other hand, we do not display ionic contributions for various values of the Zn-ion OCD since one cannot define the ionic contribution of e_{33} under non-equilibrium conditions. According to the Born–Oppenheimer approximation, the macroscopic piezoelectric tensor stems from two distinct effects: (i) the purely electronic contribution and (ii) the ionic contribution due to the atomic displacement of sublattices. In this point of view, e_{33} can be expressed as[15,16]

$$e_{33} = \left.\frac{\partial P_3}{\partial \varepsilon_3}\right|_u + \left.\frac{\partial P_3}{\partial u}\right|_{\varepsilon_3} \frac{\mathrm{d}u}{\mathrm{d}\varepsilon_3} \quad (2)$$

where u is the bond length between Zn and O_A ions along the *c*-axis. The first term in the right-hand-side of eqn (2) represents the purely electronic contribution to e_{33}, whereas the second term describes the ionic contribution. As shown in Table 1 and Fig. 2, the total e_{33} value for the $P6_3/mmc$ structure is zero. In contrast, the total (net) e_{33} value for the polar $P6_3mc$ structure is 1.01 C m^{-2}. This DFPT value which is the sum of the ionic and electronic contributions is in accordance with the experimental values.[16,52] To be more specific, the purely electronic contribution to e_{33} is -0.69 C m^{-2} while the ionic e_{33} is +1.70 C m^{-2}. This shows that the ionic contribution to e_{33} is opposite to the electronic contribution in their signs. This cancellation reflects the fact that the negatively charged electron cloud moves in the same direction as the positive Zn ions as the electron cloud follows the positively charged ionic core with some displacement between these two centres.

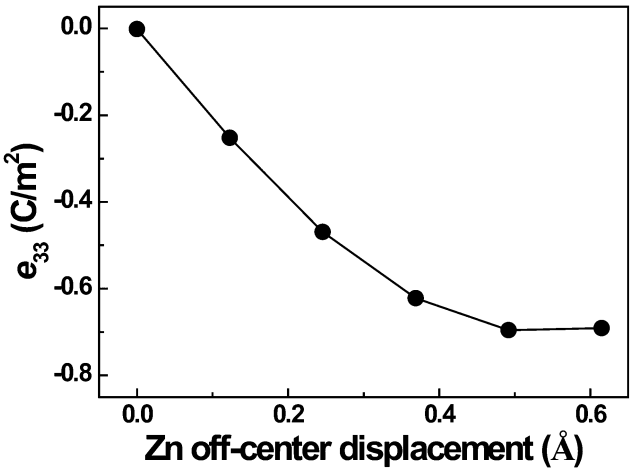

Fig. 2 Computed purely electronic contribution to e_{33} plotted as a function of the Zn-ion OCD.

The magnitude of the purely electronic contribution to e_{33} decreases with decreasing Zn-ion OCD and becomes zero at the OCD value of zero which corresponds to the $P6_3/mmc$ structure (Fig. 2). The ionic contribution is also zero at this point. We have also evaluated the *zz* component of the Bon effective charge (BEC) tensor for both $P6_3/mmc$ and $P6_3mc$ phases. The BEC tensor (*zz* component) of the Zn ion increases marginally from $\sim$1.93 to $\sim$2.04 (by 5.1%) upon the transition to the polar $P6_3mc$ structure from the nonpolar $P6_3/mmc$ structure. The enhanced BEC value of the $P6_3mc$ structure is strongly correlated with the ionic contribution to e_{33} because the BEC is represented by the term $(\partial P_3/\partial u)_{\varepsilon_3}$ in eqn (2). Thus, the Zn off-center-dependent BEC tensor is expected to correlate well with the variation in the ionic contribution to e_{33}.

In order to understand the effect of the nonpolar–polar phase transition on the electronic structure and the nature of Zn–O bonding, we compare the computed electronic band structure of the $P6_3mc$ phase with that of the $P6_3/mmc$ phase. In Fig. 3, the degree of electron occupancy is represented by circles with their size being proportional to the electron occupancy. The electron occupancy values of the Zn $4p_z$ and $3d_{z^2}$ orbitals (open circles) are much smaller than that of the O_A $2p_z$ orbital (filled green circles). Hence, we rescaled the electron occupancy values of the Zn $4p_z$ and $3d_{z^2}$ orbitals by suitably

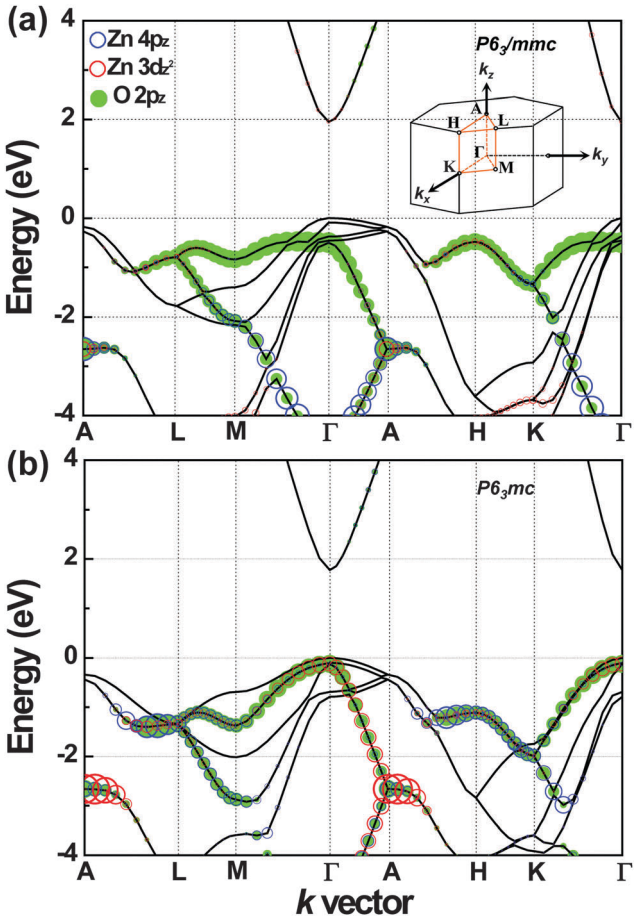

Fig. 3 Electronic band structures of hexagonal ZnO: (a) band structure of the nonpolar $P6_3/mmc$ phase along the surface $\boldsymbol{k}$ vectors of the high symmetry line of the first Brillouin zone as shown in the inset. (b) Band structure of the polar $P6_3mc$ phase.

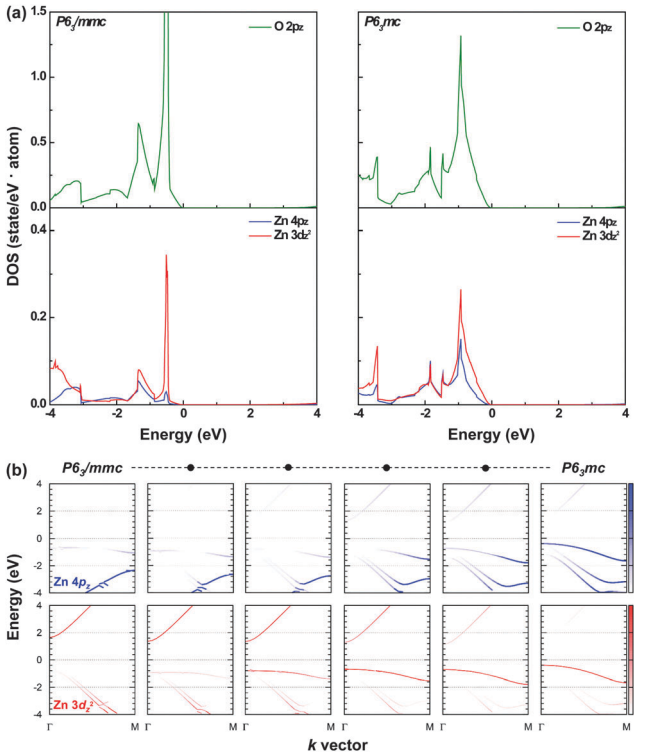

Fig. 4 (a) Comparison of the partial density of states for Zn $4p_z$, $3d_{z^2}$, and O_A $2p_z$ orbitals of the nonpolar $P6_3/mmc$ structure with those of the polar $P6_3mc$ structure. (b) The orbital-resolved band structures for selected $4p_z$ and $3d_{z^2}$ bands over the Γ–M first Brillouin zone. Here the variation of the band structure is displayed in the ascending order of the Zn-ion OCD. In the diagrams, a gradation of the line intensity was introduced to best represent the occupational density of each orbital over the Γ–M first Brillouin zone.

enlarging the occupancy values until these values were comparable to that of the O_A $2p_z$ orbital. It is interesting to notice that the electron occupancy of the Zn $3d_{z^2}$ orbital enhances remarkably upon the transition to the polar $P6_3mc$ structure (Fig. 3). The most prominent feature of the band structure for the polar $P6_3mc$ phase is a strong overlapping of the O_A $2p_z$ orbital with the Zn $3d_{z^2}$ orbital in the vicinity of symmetry point A in the first Brillouin zone.[53] Since point A corresponds to the zone boundary point at which the three components of the wave-vector ($\boldsymbol{k}$) are $(2\pi/c)(001)$, this pronounced overlapping indicates a strong covalent-bonding interaction between the Zn $3d_{z^2}$ and the O_A $2p_z$ orbitals along the c-axis or [001] of $P6_3mc$. However, we still have one puzzling problem to be clarified since the fully filled non-interacting 3d orbitals of Zn alone are not capable of forming hybridized orbitals with the O_A $2p_z$ orbitals unless the out-of-plane-type orbital self-mixing of Zn is invoked.

To resolve this controversial issue, we have examined the partial density of states (PDOS) for various atomic orbitals involved in the bonding interaction. In Fig. 4(a), we compare the orbital-resolved PDOS for O_A $2p_z$, Zn $4p_z$, and Zn $3d_{z^2}$ of the $P6_3/mmc$ structure with those of the polar $P6_3mc$ structure. The two prominent features in the PDOS are: (i) a remarkable enhancement of the Zn $4p_z$ orbital PDOS upon transition to the polar $P6_3mc$ phase and (ii) a strong overlapping of the Zn $4p_z$ orbital PDOS with the Zn $3d_{z^2}$ orbital PDOS (for an energy range between −2 and 0 eV below the valence-band top) in the $P6_3mc$ phase. These features in the PDOS, as obtained using the GGA + U method, suggest the occurrence of symmetry-allowed Zn $3d_{z^2}$–$4p_z$ orbital self-mixing in the polar $P6_3mc$ structure. Essentially the same results were obtained by using the hybrid functionals (see ESI†). This assertion of the symmetry-allowed orbital self-mixing is also in good agreement with the previous result obtained by adopting angle-resolved photoelectron spectroscopy.[54] In addition, this kind of orbital self-mixing was proposed previously for other systems, *e.g.*, a partially occupied 3d orbital ($3d^5$ or d^6) of an Fe ion[55,56] and a fully filled 4d orbital of In^{3+} in a polar hexagonally structured $InMnO_3$.[57]

In the case of the polar $P6_3mc$ phase, the PDOS results also indicate a strong overlapping of the O_A $2p_z$ orbital PDOS with the Zn $3d_{z^2}$ orbital PDOS for a wide energy range between −2 and 0 eV below the valence-band top. Combining the proposed idea of orbital self-mixing with these PDOS results, one can delineate the following bonding mechanism of Zn–O – out-of-plane-type intra-atomic $3d_{z^2}$–$4p_z$ orbital self-mixing of Zn, followed by asymmetric hybridization between the Zn $3d_{z^2}$–$4p_z$ self-mixed

orbital and the O_A $2p_z$ orbital along the *c*-axis of $P6_3mc$. This asymmetric overlapping is symmetry-allowed only for one neighboring Zn–O_A bond owing to the antisymmetric nature of the $2p_z$ orbital wavefunction along the *c*-axis.

The proposed $3d_{z^2}$–$4p_z$ orbital self-mixing of Zn can be substantiated by examining the ***k***-vector-dependent orbital-resolved band structure. In Fig. 4(b), we show the effect of the Zn-ion OCD on the band structure of ZnO for selected $3d_{z^2}$- and $4p_z$-orbital bands over the Γ–M first Brillouin zone. Here the variation in the band structure is displayed in the ascending order of the OCD (with the upper panel for $4p_z$-orbital bands and the lower panel for $3d_{z^2}$-orbital bands). The four band structures that are shown between the two extreme band structures (for $P6_3/mmc$ and $P6_3mc$ phases) correspond to the four intermediate points between the $P6_3/mmc$ state and the $P6_3mc$ state in the double-well potential [Fig. 1(c)]. In the chemical-bonding energy region (between −1.6 and −0.4 eV below the valence-band top), the degree of orbital overlapping of the Zn $3d_{z^2}$ band with the Zn $4p_z$ band is most pronounced in the polar $P6_3mc$ structure and progressively decreases as the Zn-ion OCD decreases (*i.e.*, moving from right to left). As shown in Fig. 4(b), the orbital overlapping almost vanished in the third band structure from the left and completely disappeared when the Zn-ion OCD is equal to 0 Å ($P6_3/mmc$). In other words, the piezoelectricity increases (Fig. 2) with the degree of Zn $3d_{z^2}$–$4p_z$ orbital self-mixing [Fig. 4(b)]. All these computed results thus clearly indicate that the manifestation of the *c*-axis-oriented piezoelectricity in the wurtzite ZnO is closely linked with the intra-atomic $3d_{z^2}$–$4p_z$ orbital self-mixing of Zn.

In Fig. 5, we schematically depict a sequential orbital-interaction mechanism that leads to the *c*-axis-oriented polar structure and piezoelectricity in the wurtzite ZnO. The out-of-plane-type Zn $3d_{z^2}$–$4p_z$ orbital self-mixing produces a mixed orbital ($\phi_m = c_d\phi_{3d_{z^2}} + c_p\phi_{4p_z}$ with $c_d > c_p$) having an asymmetric shape along the *c*-axis [Fig. 5(a)]. This self-mixed Zn $3d_{z^2}$–$4p_z$ orbital (ϕ_m) is now able to form an asymmetric covalent bond (ψ_{dp-p}) with one of the two neighbouring O_A $2p_z$ orbitals along the *c*-axis, not simultaneously with the two neighbouring $2p_z$ orbitals. This asymmetric covalent bonding results in spontaneous breaking of the centrosymmetric $P6_3/mmc$ state [Fig. 5(b) and 1(b)]. Fig. 5(c) depicts *c*-axis-oriented sequential MOs formed by the asymmetric covalent-bonding interaction between Zn and O_A ions in the wurtzite ZnO. In view of the present orbital-interaction mechanism, the asymmetry in the mixed orbital (ϕ_m) which is formed by the intra-atomic $3d_{z^2}$–$4p_z$ orbital self-mixing of Zn is the electronic origin of the *c*-axis-oriented piezoelectricity.

Asymmetric covalent-bonding interaction can further be visualized in real space by presenting the valence-electron charge density (VECD) profile of the bonding molecular orbitals (ψ_{dp-p}) at the highest symmetry Γ point. There is no overlapping between the VECD of the Zn ion and the VECD of the O_A ion in the $P6_3/mmc$ structure [Fig. 6(a)], which demonstrates a dominant ionic-bonding character in the Zn–O_A bond. Consequently, the VECD of the $P6_3/mmc$ structure is solely represented by the VECD of the O $2p_z$ orbital (ϕ_{2p_z}), which is in agreement with the band structure shown in Fig. 3(a). In the

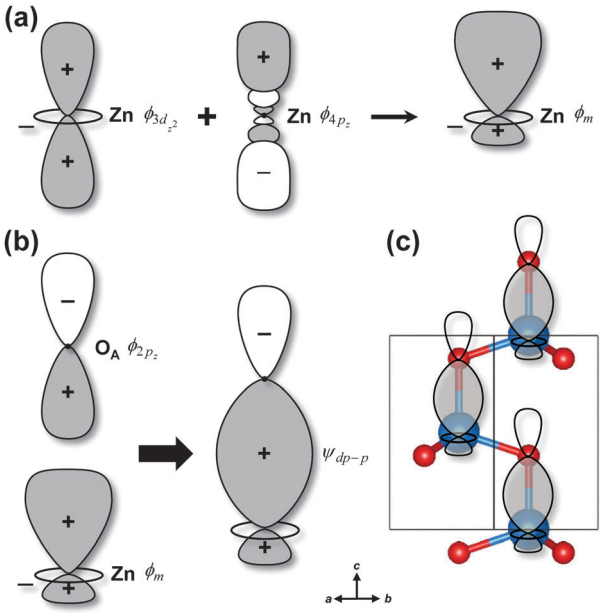

Fig. 5 Schematic orbital-interaction diagrams that illustrate bonding MOs responsible for the *c*-axis-oriented piezoelectricity: (a) intra-atomic $3d_{z^2}$–$4p_z$ orbital self-mixing of Zn. (b) Asymmetric hybridization between the Zn $3d_{z^2}$–$4p_z$ self-mixed orbital and the O_A $2p_z$ orbital along the *c*-axis of $P6_3mc$. (c) A pictorial representation of the bonding MOs for the asymmetric covalent-bonding interaction between Zn and O_A ions in the wurtzite ZnO. Blue circles denote Zn ions, whereas smaller red circles represent O_A ions.

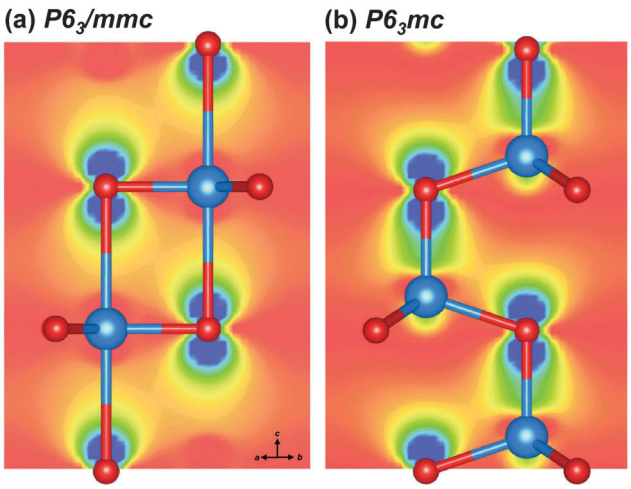

Fig. 6 Valence-electron charge density (VECD) profiles of the bonding MOs at the highest symmetry Γ point of (a) the nonpolar $P6_3/mmc$ structure and (b) the polar $P6_3mc$ structure.

$P6_3mc$ wurtzite structure, in contrast, the Zn ion moves to an asymmetric position, and there exists some covalent-bonding interaction between Zn and O_A along the *c*-axis [Fig. 6(b)]. It is interesting to notice that the VECD of the O $2p_z$ orbital becomes highly asymmetric along the *c*-axis in the polar $P6_3mc$ structure, which is in accordance with the real-space asymmetric orbital-hybridization diagram presented in Fig. 5(c). The computed valence charge density thus supports the existence of asymmetric covalent

bonding interactions between the self-mixed Zn $3d_{z^2}$–$4p_z$ orbital (ϕ_m) and one of the two neighbouring O_A $2p_z$ orbitals along the *c*-axis, which results in spontaneous breaking of the nonpolar $P6_3/mmc$ state.

4. Conclusions

We have investigated the atomic-scale origin of piezoelectricity in the polar wurtzite ZnO. For this, we evaluated the piezoelectric constants (e_{33} and e_{31}) by exploiting the DFPT calculations. The computed PDOS and orbital-resolved band structure demonstrate that the *c*-axis-oriented piezoelectricity (Fig. 2) in the wurtzite ZnO is directly associated with the degree of orbital overlapping between Zn $3d_{z^2}$ and $4p_z$ bands [Fig. 4(b)]. On the basis of further *ab initio* calculations, we propose an intriguing bonding mechanism that accounts for the *c*-axis-oriented piezoelectricity – intra-atomic $3d_{z^2}$–$4p_z$ orbital self-mixing of Zn, followed by asymmetric hybridization between the Zn $3d_{z^2}$–$4p_z$ self-mixed orbital and the O $2p_z$ orbital along the *c*-axis of the wurtzite ZnO. This mechanism can be applied to all wurtzite-based piezoelectric materials having fully filled 3d orbitals.

Acknowledgements

This work at POSTECH was supported by the National Research Foundation (NRF) Grants funded by the Korea Government (MSIP) (Grant No. NRF-2012R1A1A2041628 & NRF-2013R1A2A2A1068274). Computational resources provided by KISTI Supercomputing Centre (Project No. KSC-2013-C3-067) are gratefully acknowledged.

Notes and references

1 B. Jaffe, W. R. Cook and H. Jaffe, *Piezoelectric Ceramics*, Academic Press, London, 1971.
2 S.-E. Park and T. R. Shrout, *J. Appl. Phys.*, 1997, **82**, 1804–1811.
3 Z. L. Wang and J. Song, *Science*, 2006, **312**, 242–246.
4 Z. Kutnjak, J. Petzelt and R. Blinc, *Nature*, 2006, **441**, 956.
5 R. Yang, Y. Qin, L. Dai and Z. L. Wang, *Nat. Nanotechnol.*, 2009, **4**, 34–39.
6 M.-Y. Choi, D. Choi, M.-J. Jin, I. Kim, S.-H. Kim, J.-Y. Choi, S. Y. Lee, J. M. Kim and S.-W. Kim, *Adv. Mater.*, 2009, **21**, 2185–2189.
7 Y. Zhang, Y. Liu and Z. L. Wang, *Adv. Mater.*, 2011, **23**, 3004–3013.
8 G. Zhang, X. Luo, Y. Zheng and B. Wang, *Phys. Chem. Chem. Phys.*, 2012, **14**, 7051–7058.
9 S. Roberts, *Phys. Rev.*, 1947, **71**, 890–895.
10 R. E. Cohen, *Nature*, 1992, **358**, 136–139.
11 R. Guo, L. E. Cross, S.-E. Park, B. Noheda, D. E. Cox and G. Shirane, *Phys. Rev. Lett.*, 2000, **84**, 5423–5426.
12 S. W. Choi, R. T. R. Shrout, S. J. Jang and A. S. Bhalla, *Ferroelectrics*, 1989, **100**, 29–38.
13 H. Fu and R. E. Cohen, *Nature*, 2000, **403**, 281–283.
14 J. Wang, J. B. Neaton, H. Zheng, V. Nagarajan, S. B. Ogale, B. Liu, D. Viehland, V. Vaithyanathan, D. G. Schlom, U. V. Waghmare, N. A. Spaldin, K. M. Rabe, M. Wuttig and R. Ramesh, *Science*, 2003, **299**, 1719–1722.
15 F. Bernardini, V. Fiorentini and D. Vanderbilt, *Phys. Rev. B: Condens. Matter Mater. Phys.*, 1997, **56**, R10024–R10027.
16 A. Dal Corso, M. Posternak, R. Resta and A. Baldereschi, *Phys. Rev. B: Condens. Matter Mater. Phys.*, 1994, **50**, 10715–10721.
17 N. A. Hill and U. Waghmare, *Phys. Rev. B: Condens. Matter Mater. Phys.*, 2000, **62**, 8802–8810.
18 A. Onodera and M. Takesada, *Advances in Ferroelectrics*, INTECH, Rijeka, 2012, ch. 11.
19 Q. Yang, Y. Wu, Y. Liu, C. Pan and Z. L. Wang, *Phys. Chem. Chem. Phys.*, 2014, **16**, 2790–2800.
20 P. Gopal and N. A. Spaldin, *J. Electron. Mater.*, 2006, **35**, 538–542.
21 M. H. Huang, Y. Wu, H. Feick, N. Tran, E. Weber and P. Yang, *Adv. Mater.*, 2001, **13**, 113–116.
22 Z. W. Pan, Z. R. Dai and Z. L. Wang, *Science*, 2001, **291**, 1947–1949.
23 X. Y. Kong and Z. L. Wang, *Nano Lett.*, 2003, **3**, 1625–1631.
24 X. Y. Kong, Y. Ding and Z. L. Wang, *Science*, 2004, **303**, 1348–1351.
25 W. L. Hughes and Z. L. Wang, *J. Am. Chem. Soc.*, 2004, **126**, 6703–6709.
26 P. X. Gao, Y. Ding, W. Mai, W. L. Hughes, C. Lao and Z. L. Wang, *Science*, 2005, **309**, 1700–1704.
27 R. Zhu, D. Wang, S. Xiang, Z. Zhou and X. Ye, *Nanotechnology*, 2008, **19**, 285712.
28 R. Agrawal and H. D. Espinosa, *Nano Lett.*, 2011, **11**, 786–790.
29 A. R. H. Preston, B. J. Ruck, L. F. J. Piper, A. DeMasi, K. E. Smith, A. Schleife, F. Fuchs, F. Bechstedt, J. Chai and S. M. Durbin, *Phys. Rev. B: Condens. Matter Mater. Phys.*, 2008, **78**, 155114.
30 Y. Noel, C. M. Zicovich-Wilson, B. Civalleri, Ph. D'Arco and R. Dovesi, *Phys. Rev. B: Condens. Matter Mater. Phys.*, 2001, **65**, 014111.
31 M. Catti, Y. Noel and R. Dovesi, *J. Phys. Chem. Solids*, 2003, **64**, 2183–2190.
32 X. Wu, D. Vanderbilt and D. R. Hamann, *Phys. Rev. B: Condens. Matter Mater. Phys.*, 2005, **72**, 035105.
33 Z. C. Tu and X. Hu, *Phys. Rev. B: Condens. Matter Mater. Phys.*, 2006, **74**, 035434.
34 P. E. Blöchl, *Phys. Rev. B: Condens. Matter Mater. Phys.*, 1994, **50**, 17953–17979.
35 G. Kresse and D. Joubert, *Phys. Rev. B: Condens. Matter Mater. Phys.*, 1999, **59**, 1758–1775.
36 G. Kresse and J. Hafner, *Phys. Rev. B: Condens. Matter Mater. Phys.*, 1993, **47**, 558–561.
37 G. Kresse and J. Furthmüller, *Phys. Rev. B: Condens. Matter Mater. Phys.*, 1996, **54**, 11169–11186.
38 H. J. Monkhorst and J. D. Pack, *Phys. Rev. B: Condens. Matter Mater. Phys.*, 1976, **13**, 5188–5192.
39 P. E. Blöchl, O. Jepsen and O. K. Andersen, *Phys. Rev. B: Condens. Matter Mater. Phys.*, 1994, **49**, 16223–16233.

40 W. Ranke, *Solid State Commun.*, 1976, **19**, 685–688.
41 C. Elsässer, M. Fähnle, C. T. Chan and K. M. Ho, *Phys. Rev. B: Condens. Matter Mater. Phys.*, 1994, **49**, 13975–13978.
42 X. Gonze, *Phys. Rev. A: At., Mol., Opt. Phys.*, 1995, **52**, 1086–1095; X. Gonze, *Phys. Rev. A: At., Mol., Opt. Phys.*, 1995, **52**, 1096–1114; X. Gonze, *Phys. Rev. B: Condens. Matter Mater. Phys.*, 1997, **55**, 10337–10354; X. Gonze and C. Lee, *Phys. Rev. B: Condens. Matter Mater. Phys.*, 1997, **55**, 10355–10368.
43 S. Baroni, S. de Gironcoli, A. D. Corso and P. Giannozzi, *Rev. Mod. Phys.*, 2001, **73**, 515–562.
44 D. R. Hamann, X. Wu, K. M. Rabe and D. Vanderbilt, *Phys. Rev. B: Condens. Matter Mater. Phys.*, 2005, **71**, 035117.
45 J. Albertsson, S. C. Abrahams and Å. Kvick, *Acta Crystallogr., Sect. B: Struct. Sci.*, 1989, **45**, 34–40.
46 F. Claeyssens, C. L. Freeman, N. L. Allan, Y. Sun, M. N. R. Ashfold and J. H. Harding, *J. Mater. Chem.*, 2005, **15**, 139–148.
47 R. B. Capaz, H. Lim and J. D. Joannopoulos, *Phys. Rev. B: Condens. Matter Mater. Phys.*, 1995, **51**, 17755–17757.
48 J. Goniakowski, C. Noguera and L. Giordano, *Phys. Rev. Lett.*, 2004, **93**, 215702.
49 P.-Y. Prodhomme, A. Beya-Wakata and G. Bester, *Phys. Rev. B: Condens. Matter Mater. Phys.*, 2013, **88**, 121304.
50 H. Y. S. Al-Zahrani, J. Pal and M. A. Migliorato, *Nano Energy*, 2013, **2**, 1214–1217.
51 R. D. King-Smith and D. Vanderbilt, *Phys. Rev. B: Condens. Matter Mater. Phys.*, 1993, **47**, 1651–1654; D. Vanderbilt and R. D. King-Smith, *Phys. Rev. B: Condens. Matter Mater. Phys.*, 1993, **48**, 4442–4455.
52 I. B. Kobiakov, *Solid State Commun.*, 1980, **35**, 305–310.
53 S.-H. Wei and A. Zunger, *Phys. Rev. B: Condens. Matter Mater. Phys.*, 1988, **37**, 8958–8981.
54 R. T. Girard, O. Tjernberg, G. Chiaia, S. Söderhom, U. O. Karlsson, C. Wigren, H. Nylén and I. Lindau, *Surf. Sci.*, 1997, **373**, 409–417.
55 T. E. Westre, P. Kennepohl, J. G. DeWitt, B. Hedman, K. O. Hodgson and E. I. Solomon, *J. Am. Chem. Soc.*, 1997, **119**, 6297–6314.
56 J.-H. Lee, H. J. Choi, D. Lee, M. G. Kim, C. W. Bark, S. Ryu, M.-A. Oak and H. M. Jang, *Phys. Rev. B: Condens. Matter Mater. Phys.*, 2010, **82**, 045113.
57 M.-A. Oak, J.-H. Lee, H. M. Jang, J. S. Goh, H. J. Choi and J. F. Scott, *Phys. Rev. Lett.*, 2011, **106**, 047601.